chemosensors

Article

Emergency Wound Infection Monitoring and Treatment Based on Wearable Electrochemical Detection and Drug Release with Conductive Hydrogel

Shaopeng Wang [1,2,†], Songsong Huang [1,†], Qian Chen [1,2], Yanjun Li [1,3], Liyang Duan [1], Zhi Yu [1], Weixia Li [1,2], Hui Luo [1], Shuang Li [2], Bin Fan [1,3,*] and Zetao Chen [1,3,*]

[1] School of Disaster and Emergency Medicine, Tianjin University, Tianjin 300072, China
[2] Medical College, Tianjin University, Tianjin 300072, China
[3] Wenzhou Safety (Emergency) Institute of Tianjin University, Wenzhou 325026, China
* Correspondence: fanbin911@126.com (B.F.); zetaochen@tju.edu.cn (Z.C.)
† These authors contributed equally to this work.

Abstract

At emergency sites, bacteria in the environment can cause secondary wound infections. Timely treatment of infected wounds can improve the prognosis. In this study, we designed a closed-loop system for real-time wound infection monitoring and electronically controlled drug release, enabling rapid and stable deployment at disaster sites. Multilayer screen-printed electrodes were developed to detect uric acid (UA), pH, and temperature biomarkers. The electrode's outermost layer was shielded by a zwitterionic conductive hydrogel (Gel) to prevent environmental interference and achieve systematic antibacterial protection through in situ reduction of silver nanoparticles (AgNPs) on its surface. For rapid and efficient drug delivery, amikacin (Ami) loaded cationic liposomes (Lipo) embedded in the zwitterionic conductive hydrogel (Gel-Lipo@Ami) were integrated as the core therapeutic carrier. This closed-loop system provides timely infection detection and enables in situ treatment during emergency rescues.

Keywords: wound infection monitoring; conductive hydrogel; electronically controlled drug release; wearable sensors

check for updates

Received: 21 May 2025
Revised: 5 July 2025
Accepted: 15 July 2025
Published: 21 July 2025

Citation: Wang, S.; Huang, S.; Chen, Q.; Li, Y.; Duan, L.; Yu, Z.; Li, W.; Luo, H.; Li, S.; Fan, B.; et al. Emergency Wound Infection Monitoring and Treatment Based on Wearable Electrochemical Detection and Drug Release with Conductive Hydrogel. *Chemosensors* **2025**, *13*, 267. https://doi.org/10.3390/chemosensors13070267

Copyright: © 2025 by the authors. Licensee MDPI, Basel, Switzerland. This article is an open access article distributed under the terms and conditions of the Creative Commons Attribution (CC BY) license (https://creativecommons.org/licenses/by/4.0/).

1. Introduction

Wound infection is characterized by a breach of the skin's integrity and the infiltration, replication, and eradication of various pathogens such as bacteria, fungi, and viruses in the affected area. This impedes wound healing, triggers local and systemic inflammatory responses, significantly impairs the healing process, and poses a risk of amputation and mortality [1,2]. Globally, bacterial infections rank as the second leading cause of death, contributing to one in eight fatalities [3]. In emergency medical scenarios, patients often struggle to promptly identify the severity of wounds and detect infections due to external factors, complicating subsequent treatment [4]. Infections stemming from environmental microorganisms penetrating the body can provoke inflammation and delay wound recovery [5], necessitating antimicrobial intervention during emergency medical interventions [6]. Consequently, there is a pressing need for a timely and efficacious approach to monitor and manage wound infections.

Recent advancements in biosensing and flexible electronics have facilitated the development of biosensing-controlled therapeutic systems, addressing clinical challenges in

emergency medical settings [7]. Integrated flexible electrochemical sensors detect markers in wounds, such as pH, uric acid (UA), oxygenation, inflammatory factors, bacteria, and bacterial metabolites [8–10]. Elevated skin temperature in localized areas is indicative of infection in and around the wound [11]. Physiologically, normal skin maintains an acidic pH range of 4 to 6, which shifts towards alkalinity upon wound formation and further increases in the presence of infection due to microbial proliferation [12,13]. The concentration of UA at wound sites typically ranges from 220 to 750 μM, correlating with the severity of the wound [14]. In infected wounds, bacterial activity can lower UA levels in exudate to around 200 μM [15]. Monitoring UA concentration in wound exudate serves as a preliminary assessment of wound status. However, the complex emergency environment poses a risk of damage to unprotected electrodes at the rescue site, potentially compromising data accuracy. Therefore, safeguarding the detection electrode with wound dressing is essential to enhance its resistance to environmental interference and ensure monitoring data precision [16–18].

Stimulus-responsive hydrogels are extensively utilized in wound infection treatment due to their intelligent responsiveness and promising applications [19,20]. By integrating sensors with these hydrogels, drug release control can be achieved via electrical, magnetic, pH, and temperature stimuli [21–23]. Among these, electro-responsive hydrogels offer the most straightforward control over drug release [24]. Nevertheless, current systems combining monitoring and treatment face limitations in emergency scenarios. The presence of bacteria in natural settings poses a significant concern, especially in disaster contexts. For example, gas gangrene, a severe infection resulting from *Clostridium perfringens* invasion of skin tissue, is frequently observed in earthquake-related incidents [25,26]. Hence, wound dressings for therapeutic purposes need to possess antimicrobial properties to protect against environmental bacteria and reduce the risk of secondary infections. Notably, zwitterionic gels derived from [2-(methacryloyloxy)ethyl] dimethyl-(3-sulfopropyl)ammonium hydroxide (SBMA) exhibit favorable electrical conductivity and biocompatibility, making them a popular choice for wound infection treatment [27,28]. Furthermore, the incorporation of antimicrobial agents like AgNPs into Gel presents a promising approach for ensuring antimicrobial protection in the treatment module. Additionally, the controlled release of drugs is a critical consideration. In drug delivery systems, the combination of hydrogels and Lipo is a prevalent method for in vitro delivery. Drugs such as Ami and vancomycin are suitable options for localized administration in skin trauma cases [29].

The integration of real-time wound infection detection and in situ therapy modules has undergone significant refinement in recent years, facilitating the identification of wound infection markers and controlled drug release [30]. Detecting wound infection early can help reduce the risk of antibiotic misuse, leading to drug-resistant bacteria. This approach allows for targeted local treatments instead of systemic oral medication, thereby enhancing treatment efficacy and minimizing adverse outcomes [31]. In this study, we introduced a flexible wearable device that combines wound infection monitoring with an electrically controlled drug release system. A real-time sensor was developed using screen printing technology to monitor levels of uric acid, pH, and temperature in wounds. A Gel was created through thermal polymerization of zwitterionic polymer SBMA and N-(2-hydroxyethyl)-2-acrylamide (HEAA) to enable controlled drug release. AgNPs with broad-spectrum antimicrobial properties were synthesized via in situ reduction on the hydrogel surface using Ag and glycyrrhizic acid (GL) reactions. Ami, a broad-spectrum antibiotic, was encapsulated in Lipo, with drug release regulated by voltage control. The drug-coated Lipo released onto the skin surface can selectively target negatively charged bacteria through electrostatic interactions, prolonging contact time with the biofilm. Wireless communication between a cell phone and a flexible printed circuit board (FPCB) enables

programming and control of the drug release process. The integrated system's visualization, anti-interference capabilities, and adjustability cater to the demand for real-time monitoring and on-site treatment of patient wounds in emergency situations.

2. Materials and Methods

2.1. Chemical and Materials

GO-COOH dispersion was purchased from XFNANO Materials Co. (Nanjing, China). Polyaniline (PANI), chloroauric acid solution ($HAuCl_4$), potassium ferricyanide ($K_3[Fe(CN_6)]$), Polyvinyl Butyral (PVB), and potassium ferrocyanide ($K_4[Fe(CN_6)]$) were purchased from Sinopharm Group Reagent Co., Ltd. (Shanghai, China). PBS, UA, glucose (Glu), ascorbic acid (AA), and creatinine solutions were purchased from Wokai Chemical Reagent Co. (Shanghai, China). Low-resistance conductive carbon ink and Ag/AgCl were purchased from Tongbai Heyuan Trading Co., Ltd. (Heyuan, China). PET was purchased from Kwong Fung Yuen Electronic Co. (Qingdao, China). Ammonium persulphate (APS), HEAA, GL, and N,N′-methylene bisacrylamide (MBA) were purchased from Kmart (Tianjin) Chemical Technology Co. (Tianjin, China). SBMA was purchased from Tianjin Hynes Optech Co. (Tianjin, China). Silver nitrate ($AgNO_3$) was purchased from Tianjin Jiangtian Chemical Technology Co. (Tianjin, China). 1-Octadecanamine was purchased from Shanghai Marel Biochemical Technology Co. (Shanghai, China). Phosphatidylcholine, and Ami were purchased from Zancheng (Tianjin) Technology Co. (Tianjin, China). Cholesterol, and Rhodamine B were purchased from Tianjin Hynes Optech Co. (Tianjin, China). *Escherichia coli* (*E. coli*), *Staphylococcus aureus* (*S. aureus*) was purchased from Beijing Zhuangmeng International Biogenetic Technology Co. (Beijing, China). L929 fibroblasts, NIH/3T3 fibroblasts, and Cell Counting Kit-8 (CCK-8) were purchased from Shanghai Jingkang Biological Engineering Co., Ltd. (Shanghai, China).

2.2. Fabrication of the Wound Infection-Detecting Electrode

Electrodes were prepared using the screen-printing technique to detect UA concentrations and pH in wounds. The counter electrode (CE) and the working electrode (WE) were made of conductive carbon ink, and the reference electrode (RE) was made of Ag/AgCl. We use modeling software of Adobe Illustrator 2022 to create electrochemical sensor templates. The outer diameter of the formwork was 35 mm × 45 mm, the inner diameter was 25 mm × 35 mm and the grid density was 250 (Figure S1). Ag/AgCl was screen-printed onto PET films as the RE using a stencil template, followed by drying at 60 °C for 3 h. The template was then replaced to print carbon ink for the CE and WE, with subsequent drying under identical conditions. The overall process schematic is shown in Figure S2. After preparation, the WE modification was performed.

2.3. Preparation and Characterization of the Sensor

GO-COOH (1 mg/mL) and $HAuCl_4$ (0.1 mM) were mixed in volume ratios (10:1, 20:1, and 30:1) dropwise on the electrode surface (100 μL) and scanned for 6 turns by cyclic voltammetry (CV) in the range of −1.5 V to 0.6 V. The detection was performed by adding 20 mM $[Fe(CN)_6]^{3-/4-}$ as a redox pair under 0.5 M KCl, with a scanning potential range of −0.4 V to 0.6 V and a scanning rate of 0.1 V/s. The modified screen-printed electrodes were rinsed, dried with water, and used for detection. The UA concentration gradient was tested using differential pulse voltammetry (DPV) with a scanning potential of −0.2 V to 0.6 V. Scanning electron microscope images of bare and modified electrodes were taken under a Sigma 500 scanning electron microscope at an accelerating voltage of 5000 V.

For pH sensors, AuNPs layers are first deposited on the working electrode by the Amperometric (i-t) method to improve conductivity. An aqueous solution containing

0.1 wt% $HAuCl_4$ in 0.5 mM Na_2SO_4 solution was prepared, and 100 µL drops were added to the working electrode. The potential was set at −0.8 V, and the deposition time was 300 s. A layer of PANI for H^+ sensing was then deposited on the AuNPs layer by i-t. The PANI layer was deposited by i-t after dissolving 0.01 M polyaniline in 0.1 M HCl solution and adding 100 µL solution to WE. The potential was set at 0.85 V, and the deposition time was 120 s. Finally, the reference electrode was modified. 50 mg NaCl and 79.1 mg Polyvinyl Butyral (PVB) were added to 1 mL of methanol, and 3 µL of solution drops were taken and added to the reference electrode, and dried at 4 °C in the absence of light for 12 h. The modified screen-printing electrode was washed with water and dried for testing. The open circuit potential-time method (OCPT) was used to measure the pH in the pH 3–8 range at room temperature and the selectivity of the electrodes.

2.4. Preparation of the Gel

AgNPs were synthesized via a photochemical reduction method utilizing GL. GL contains diglucuronic acid units with reducing capability, enabling the spontaneous reduction in Ag^+ ions to AgNPs without an external reducing agent. Under UV light, GL is first deprotonated, generating negatively charged carboxyl groups that electrostatically bind Ag^+ ions. Subsequent UV irradiation facilitates the reduction in the immobilized Ag^+ ions to AgNPs by the hydroxyl groups on GL's diglucuronic acid units [32]. Briefly, a solution containing 2 mM $AgNO_3$ and 0.5% (*w*/*v*) GL was exposed to UV light (20 W lamp) for 10 min, resulting in GL-stabilized AgNPs.

The antibacterial activity of the synthesized AgNPs was evaluated against Gram-positive (*S. aureus*) and Gram-negative (*E. coli*) bacteria. A single colony from LB agar was inoculated into LB broth and incubated for 12 h. A 1% (*v*/*v*) aliquot of this culture was then transferred to fresh LB broth and incubated for an additional 3 h. The bacterial suspension was adjusted to an optical density at 600 nm (OD_{600}) of 0.5. Aliquots (90 µL, ~5×10^8 CFU/mL) were dispensed into wells of a sterile 96-well plate. Experimental groups received 10 µL of AgNP solutions (concentrations ranging from 1 to 64 µg/mL), while blank controls received 10 µL of sterile LB medium. OD_{600} values were recorded after 24 h incubation using a microplate reader.

Prior to integrating AgNPs into the hydrogels, preliminary cytotoxicity screening was conducted to establish safe dosage ranges. L929 murine fibroblasts were selected as the primary cell model for biological evaluation of medical devices, which designate this cell line for standardized in vitro nanomaterial toxicity assessment due to the following: (1) high sensitivity to metallic ions (detection of subtle cytotoxic effects), and (2) well-characterized response databases (enabling cross-study comparisons). The biocompatibility of the AgNPs was assessed in parallel using the L929 fibroblast cell line. Rat fibroblasts (L929) were cultured in DMEM supplemented with 10% FBS and 1% penicillin–streptomycin at 37 °C in a humidified 5% CO_2 incubator. Cytotoxicity was evaluated via the CCK-8 assay. Cells were seeded into 96-well plates (5×10^4 cells/well), treated with AgNPs (1–64 µg/mL) for 24 h, then incubated with 10 µL CCK-8 reagent for 2 h. OD_{450} was measured using a multifunctional microplate reader.

A Gel functionalized with AgNPs was prepared for potential applications such as electrically controlled drug release. SBMA (1.5 g) and HEAA (500 mg) were dissolved in water, followed by the addition of GL (100 mg). The mixture was heated in an 80 °C water bath for 10 min to dissolve GL, then cooled to room temperature. APS (1.25 mL, 10 wt%) and MBA (0.25 mL, 2 wt%) were added under rapid stirring. The solution was poured into a glass mold, sealed, and reacted at 70 °C for 2 h to form the initial hydrogel. After storage at 4 °C for 24 h, the hydrogels were removed from the molds. To impart antimicrobial properties, the hydrogel surface was uniformly coated with 1 wt% $AgNO_3$ solution and

exposed to a 20 W UV lamp for 10 min. This utilized the same $AgNO_3$/GL photochemical reduction mechanism described above to generate AgNPs in situ on the hydrogel surface, yielding the final Gel. A comprehensive flowchart detailing the step-by-step preparation procedures described in this section is provided as Figure S3a.

2.5. Preparation and Characterization of the Treatment Module

Lipo embedded with Ami (Lipo@Ami) was prepared as follows: Egg yolk lecithin (12 mg), cholesterol (1.5 mg), 1-Octadecanamine (1.5 mg), Ami (2.25 mg), and ethanol (2 mL) were combined in a beaker and magnetically stirred (400 rpm, 45 min, room temperature). This mixture was added dropwise (using a 200 μL pipette) into a beaker containing 8 mL of water placed in a thermostatically heated magnetic stirrer set at 35 °C. (For rhodamine B-labeled Lipo, 8 mg rhodamine B was added at this stage under light-protected conditions.) Stirring (400 rpm) continued for 2 h after the addition was complete. The solution was removed once no ethanol odor was detectable. Lipo@Ami was obtained by filtration through a 0.22 μm pore size, 13 mm diameter filter membrane. (Details of the Ami encapsulation rate test are provided in the Supplementary Materials.)

The degree of swelling of the hydrogel samples was studied using the weight method. Pre-weighed hydrogel samples were incubated in water for specific durations (1 h, 4 h, 8 h, 24 h). After removing excess surface water, the swollen hydrogels were weighed again. The swelling ratio (M_1/M_0) was calculated, where M_1 is the mass at swelling equilibrium and M_0 is the initial mass before swelling.

To combine Gel with Lipo@Ami, the Gel was sealed and incubated with 16 mL of rhodamine B-labeled Lipo@Ami at 4 °C for 24 h. This resulted in Gel-Lipo@Ami. A comprehensive flowchart detailing the step-by-step preparation procedures described in this section is provided as Figure S3b.

2.6. Quantitative Drug Release in the Treatment Module

The drug released by Gel-Lipo@Ami was quantitatively analyzed by fluorescence imaging. First, a controllable voltage excitation was applied to Gel-Lipo@Ami by an FPCB, and Rhodamine B labeled Lipo@Ami was collected on a slide. Fluorescent images of the sample were captured with an identical exposure time and exposure intensity. The images were analyzed and processed using ImageJ 1.54g, and the overall fluorescence intensity of each group was obtained. The natural drug release of Gel-Lipo@Ami with electrical stimulation and Lipo@Ami without electrical stimulation was calculated using the global fluorescence intensity of 10 μL Lipo@Ami as a reference point. The optimal intensity and duration of electrical stimulation were investigated by implementing a controlled experiment.

2.7. Antibacterial Activity and Biocompatibility Testing

Given that wound dressings directly contact human tissue, the biocompatibility of biomaterials is essential for maintaining cell viability and proliferation. Since fibroblast proliferation is central to wound healing, NIH/3T3 fibroblasts were selected to evaluate the cytocompatibility of hydrogel dressings. Following the protocol outlined in Section 2.4, the CCK-8 assay was employed to assess the impact of hydrogels on NIH/3T3 fibroblast proliferation and viability. First, hydrogel samples were sterilized under UV irradiation. The hydrogels were incubated with PBS buffer at 37 °C for 24 h to obtain hydrogel extract solutions. After filtration through disposable sterile filters, extracts were diluted to 10 mg/mL. Cells were cultured in DMEM supplemented with 10% FBS, 1% penicillin, and 1% streptomycin. Aliquots of 90 μL NIH/3T3 cell suspension (5×10^4 cells/mL) were seeded into 96-well plates and incubated at 37 °C with 5% CO_2 for 24 h. Subsequently, hydrogel extracts were added to each well for co-culture. At 0, 24, and 48 h, 10 μL CCK-8

solution was added per well. After 4 h incubation, the OD_{450} was measured using a microplate reader. Here, $OD_{control}$ denotes the absorbance of cells cultured in control medium (without hydrogel extract), while $OD_{treated}$ represents cells cultured with hydrogel extracts.

To verify the antibacterial activity of hydrogel extracts against *S. aureus* and *E. coli*, assessments followed the AgNPs methodology described in Section 2.4. Briefly, activated bacterial suspensions were adjusted to OD_{600} = 0.5 and dispensed into sterile 96-well plates. Experimental groups received 10 μL of hydrogel extract, while blank control wells received 10 μL of sterile LB medium. After 24 h incubation at 37 °C, OD_{600} was measured directly using a microplate reader.

2.8. In Vivo Wound Healing

Animal experiments were approved by the Experimental Animal Ethics Committee of Tianjin University (20250113001). *E. coli* was passed twice to obtain *E. coli* (OD_{600} is about 0.4 (1×10^8 CFU/mL)). After three days of parallel rearing of SD rats, rats were anesthetized (isoflurane) by gas, and a circular wound of 1.5 cm in diameter was made on each side of the spine (up to the level of the tendon membrane). Each wound was titrated with 100 μL of 10^8 CFU/mL *E. coli*, and white pus was observed in rat wounds after 48 h, indicating successful wound modeling. An integrated system detected UA levels in rat exudate, and the data were recorded wirelessly. Accelerated drug release from Gel-Lipo@Ami was accelerated by applying electrical stimulation through the integrated system. After successful wound modeling, the treatment group applied a 3 V voltage excitation to the Gel-Lipo@Ami affixed to the wound for 10 min every day, and this treatment lasted for five days. Wound healing data were recorded daily for the untreated and treated groups before and after treatment. After 15 days, rats were euthanized, and the infected skin tissues of wounds and the heart, liver, spleen, lungs, and kidneys were sampled. Tissue samples were washed with 0.9% saline and then fixed in 4% paraformaldehyde for tissue sectioning and H&E staining.

3. Results

3.1. Wound Infection Detection and Treatment System Overview

We have designed a sophisticated closed-loop system for promptly monitoring and treating wound infections, as shown in Figure 1. This system features a layered architecture, comprising a multi-layer electrode integrated with Gel as its core component. The coating layer consists of a Gel responsible for controlled drug release, while the upper layer incorporates a screen-printed electrode for monitoring and voltage application, and the top layer is a modified Gel. The monitoring module primarily incorporates UA and pH screen-printed electrodes with a signal amplification approach utilizing the large specific surface area property of AuNPs to enhance current signal detection. This setup enables the real-time monitoring of UA and pH levels in wound exudate. Additionally, a temperature module integrated into an FPCB is employed to detect wound temperature, utilizing the M1117 temperature sensor to achieve high-sensitivity temperature measurements with an accuracy of 0.1 degrees. The monitoring electrode is enhanced and regulated by the FPCB, facilitating the application of adjustable voltage excitation during wound infection monitoring. The treatment module's core component is a Gel comprising zwitterionic polymerization. Lipo loaded with Ami is incorporated through incubation for effective treatment delivery.

The treatment module designed for emergency scenarios features a layered structure with a Gel serving as a protective and antibacterial coating for the electrode. AgNPs are *in situ* reduced within the upper hydrogel through the reaction of GL and Ag^+, imparting antibacterial properties to the system [33]. Critically, when integrated sensors detect infec-

tion biomarkers (UA < 220 μM, pH > 6, or elevated temperature), the microcontroller unit (MCU) triggers a digital-to-analog converter (DAC) to apply a programmed voltage to the hydrogel. Under this electrical stimulation, drug-loaded Lipo directionally migrate toward the oppositely charged electrode. Simultaneously, the Gel undergoes micro-contraction and dehydration, synergistically promoting drug release. The electric field further facilitates directional diffusion of charged therapeutics to target sites, enabling precise, rapid delivery. As shown in Figure 1, applying a positive potential to the hydrogel and grounding its edge causes the drug-loaded hydrogel to undergo micro-contraction and dehydration. The positively charged drug-loaded Lipo moves toward the negative region, achieving drug release. When wound healing is detected, the potential reverses, stopping drug release [34–36]. Ami acts on the ribosomes of bacteria through percutaneous penetration, inhibiting bacterial protein synthesis and causing cell death [37]. The combination of broad-spectrum antibiotics and Lipo extends drug retention at wound sites, and animal experiments have verified the therapeutic effect [38,39]. The system, comprising flexible materials for comfortable wear, represents an intelligent solution tailored for emergency situations.

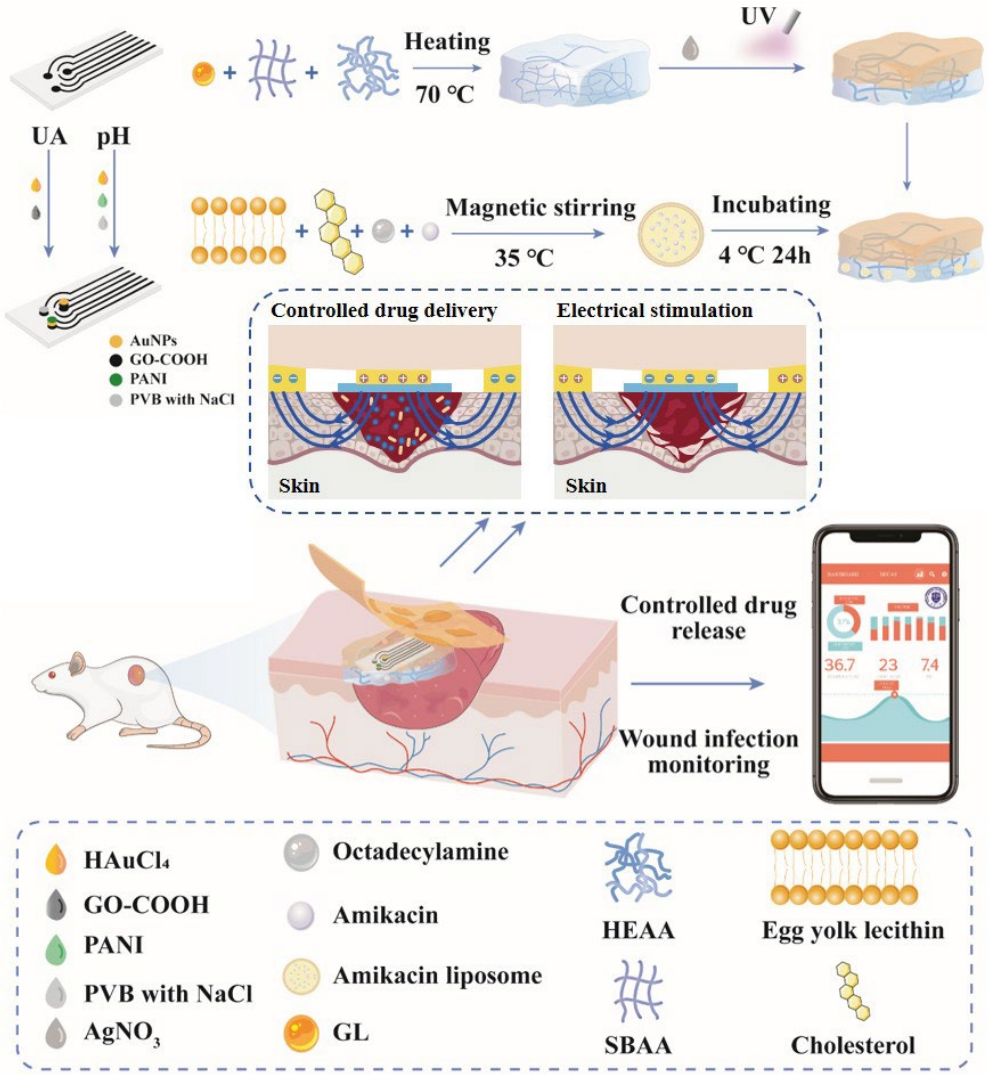


Figure 1. Integrated system diagram. It includes electrode modification, preparation of Gel, preparation of coated Lipo, system combination, detection of wound infections, and an electronically controlled drug release process.

3.2. Modification of the Integrated Screen-Printed Electrodes

Hypoxia at the wound site may result from ulcer formation caused by wound infections, leading to adenosine triphosphate (ATP) depletion and subsequent accumulation of purine metabolites. Xanthine oxidoreductase can convert hypoxanthine to uric acid through a series of reactions and release reactive oxygen species (ROS) simultaneously [40]. Further studies found that elevated trauma fluid uric acid was positively correlated with elevated trauma severity [14]. Traumatic exudate has been reported to contain uric acid concentrations ranging from 220 to 750 μM, with levels below 220 μM potentially indicating infection by pathogenic bacterial strains [15] such as *E. coli*, *S. aureus*, *Pseudomonas aeruginosa* (PA), *Proteus mirabilis*, and *Corynebacterium* spp. [41–43]. The human body lacks an enzyme to metabolize uric acid, while certain bacteria can convert uric acid to 5-hydroxyisouric acid via uricase [44], lowering UA levels to 200 μM [45]. Therefore, a UA concentration in wound exudates below the standard threshold can be considered a bacterial infection, and an increase in UA concentration within the standard threshold can be regarded as an increase in wound severity. To monitor wound infections, assess wound severity, and detect the presence of infection, a signal amplification strategy was employed to fabricate UA electrodes. Preliminary determination of wound severity and infection presence was based on UA concentration measurements. To enhance the accuracy of wound assessment and reduce errors associated with single-target detection, temperature and pH levels at the wound site were also measured using a multi-channel integrated sensing system, enabling a comprehensive and precise diagnosis of wound infections.

Gold nanoparticles were chosen for signal amplification due to their high specific surface area. In the electrocatalytic process, gold nanoparticles were deposited on the WE through a reduction–oxidation reaction between partially reduced graphene oxide carboxylate and $HAuCl_4$. A commonly cited ratio in the literature is 10:1 for GO-COOH to $HAuCl_4$ [46]. However, to ensure an adequate number of active sites on the graphene oxide surface to support the gold nanoparticles without causing aggregation, an appropriate increase in GO-COOH may be necessary. The proportional parameters of electrode modification were optimized to achieve the optimal results. The impact of different volume ratios of GO-COOH and $HAuCl_4$ on the electrochemical response of the modified electrodes was investigated using volume ratios of 10:1, 20:1, and 30:1 (Figure S4). GO-COOH and $HAuCl_4$ were added dropwise simultaneously to the WE and tested by CV. Due to oxygen-containing functional groups in GO-COOH, GO-COOH adsorbed on the electrode surface was gradually reduced to rGO-COOH [46]. Then, rGO-COOH will reduce AuNPs from the mixed GO-COOH/$HAuCl_4$ solution. Figure 2a shows the reduction of Au^{3+} to Au^0 in the mixture, and the reduction peaks indicate the successful reduction in AuNPs. After completing the modification, the electrode was cleaned and dried. Then, the performance of the modified electrode was tested by dropping a couple of ferricyanide/ferrocyanide solutions onto the working electrode.

CV tests were conducted on three electrodes with varying proportions of modification, as well as on the bare electrode, as depicted in Figure 2b. The modified electrodes exhibited increased peak currents for $[Fe(CN)_6]^{3+}/[Fe(CN)_6]^{4+}$ compared to the bare electrode, with more pronounced enhancements observed at ratios of 10:1 and 20:1, leading to an increase from 0.25 μA to 0.4 μA. Furthermore, the peak-to-peak separation varied between the bare electrode and those modified with different ratios of GO-COOH/AuNPs, indicating the modification of the electrode by nanomaterials. The electrocatalytic performance of the GO-COOH/AuNPs nanocomposite-modified electrode surpassed that of the unmodified electrode. SEM images in Figure 2c,d revealed that the rough surface of the unmodified electrode resulted in a suboptimal current response, while the modified electrode exhibited a distinct rGO-COOH lamellar structure with dispersed AuNPs of approximately 100 nm

in diameter. DPV was employed to detect UA solutions within the concentration range of 100 μM to 1 mM to assess the sensor's ability to detect UA and monitor concentration changes. As shown in Figure 2e, the DPV peak current for UA increases with increasing UA concentration, with all peaks occurring around 0.2 V. The linear fitting of the peak currents under the concentration gradient is presented in Figure 2f. For the 20:1 ratio, the linear regression equation for UA detection is $Y = 1.668 \times 10^{-8}X + 1.804 \times 10^{-6}$, with $R^2 = 0.9948$. (Linear regression equations for the 10:1 and 30:1 ratios are shown in Figure S4.) While the CV results indicated similar peak currents for the 10:1 and 20:1 ratios, both higher than that of the 30:1 ratio, the sensitivity achieved with the 20:1 ratio was significantly higher than that of both the 10:1 and 30:1 ratios. By comparing the CV, SEM, DPV, and linear fitting data for the three modification ratios, a GO-COOH:$HAuCl_4$ volume ratio of 20:1 was selected as the optimal electrode modification scheme for subsequent experiments. This selection was based on the observation that at a 10:1 ratio, the number of AuNPs is relatively low, resulting in insufficient active sites on the electrode surface. On the other hand, a 30:1 ratio leads to an excess of GO-COOH, which causes the AuNPs to aggregate and reduces the overall catalytic performance. The 20:1 ratio strikes a balance, offering the best combination of sensitivity, selectivity, stability, and linear range. This makes it the ideal choice for enhancing the electrode's performance in subsequent experiments.

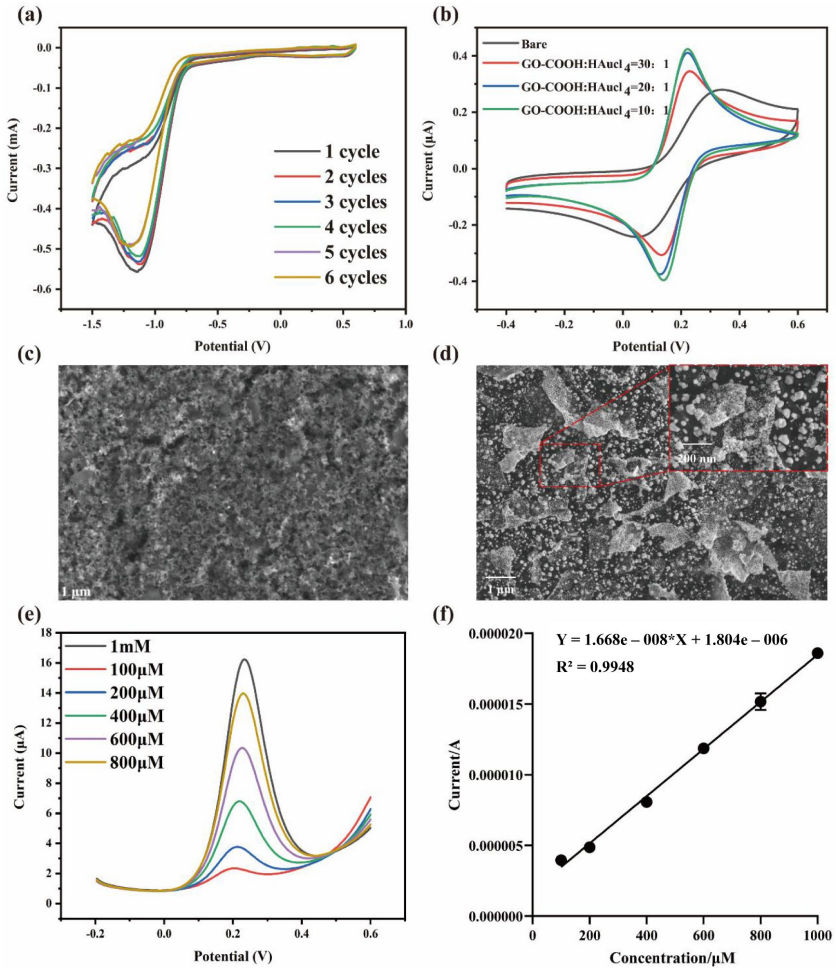


Figure 2. Electrode optimization and characterization. (**a**) Cyclic voltammograms of deposited AuNPs. (**b**) Characterization of the electrode. Comparison of different proportion modifications with bare electrodes. (**c**) SEM images of bare electrode and (**d**) reduced graphene oxide and AuNPs-modified electrode. (**e**) The diagram shows the differential pulse voltammetry measurement of UA at different concentrations. (**f**) Linear fitting curve of uric acid concentration.

Since wound exudate contains AA, Glu, creatinine, and other possible substances in addition to UA [47–49], we measured UA as well as interfering molecules in real samples and recorded DPV response currents (Figure 3a). To investigate the selectivity of UA detection, the effects of 50 μM AA, 200 μM GL, and 100 μM creatinine in wound exudate were determined. It can be seen that the signal response of the interfering molecule changes very little, indicating reasonable specificity of the UA sensor. UA detection in real samples is shown in Figure 3b. The oxidation peak of UA was observed at 0.2 V.

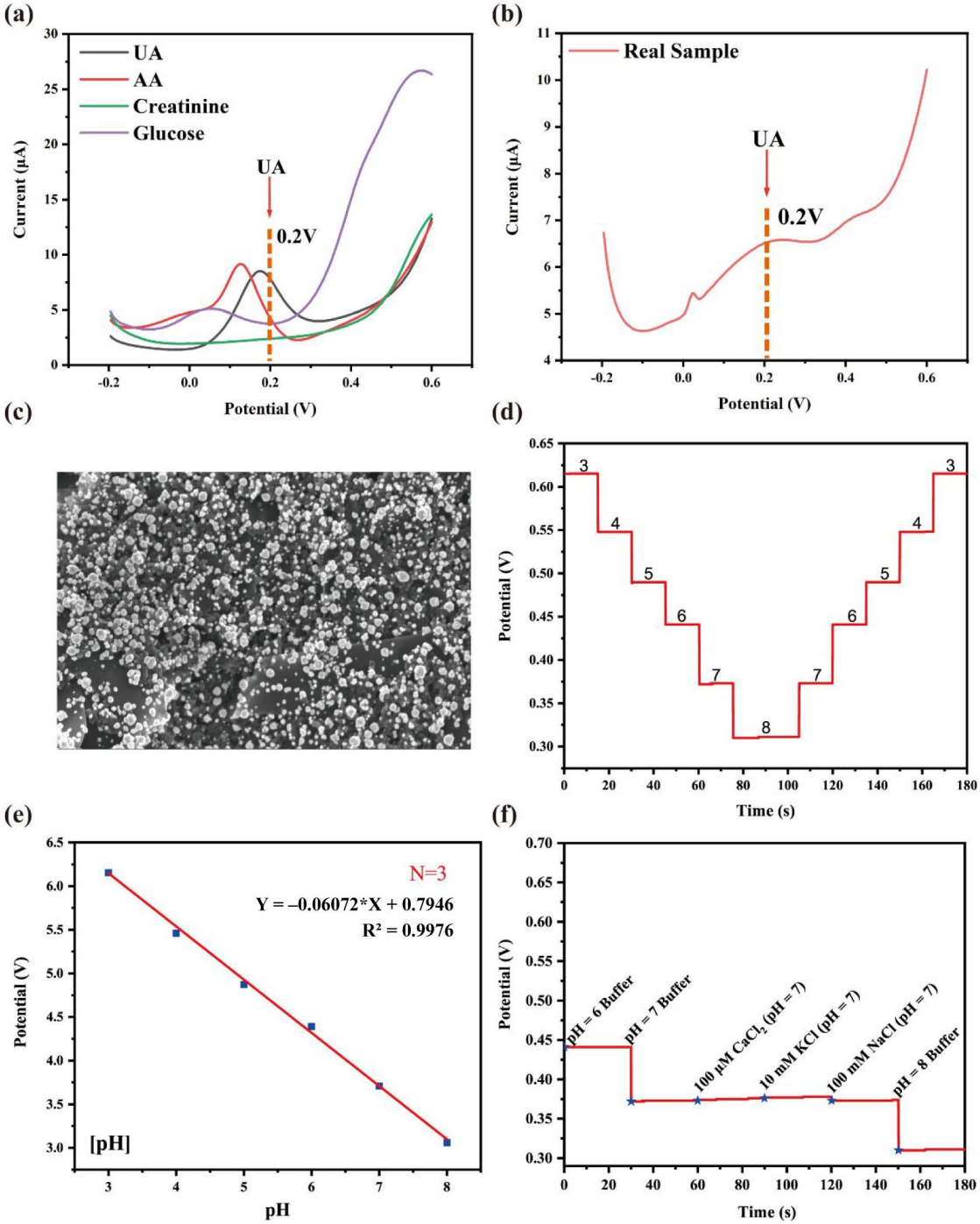


Figure 3. UA detection of the electrode. (**a**) The sensor's specificity was detected by differential pulse voltammetry. (**b**) Detection of UA in a real sample. (**c**) Chronoelectric deposition of AuNPs. (**d**) The detection of pH in the range of pH 3–8. (**e**) Linearity of the pH detection. (**f**) Specificity of pH detection with WE.

Following UA detection, pH measurements were conducted at room temperature within the pH range of 3–8. Firstly, AuNPs were electrochemically deposited on WE, which could be verified by the SEM image in Figure 3c. After the deposition of PANI on the WE and modification of PVB with NaCl on the RE, H^+ was detected by deprotonation on the PANI surface. As shown in Figure 3d, standard buffers were measured continuously in the pH 3 to pH 8 (forward) and pH 8 to pH 3 (reverse) ranges. The results of forward and reverse measurements are basically the same, indicating that the prepared pH electrode has good reversibility and repeatability, and the calculation error was repeated three times in all experiments. As shown in Figure 3e, the linearity of the pH detection was calculated using the least squares method, and the calibration curve equation was fitted. Compared to the standard parameter of 59.2 mV in the Nernst equation, the stable voltage output of the sensor also shows near-Nernst behavior, with a sensitivity of 60.07 mV per tenfold H^+ concentration. To ascertain the pH electrode's specificity, the presence of Ca^{2+}, K^+, Na^+, and other electrolyte ions in the wound exudate was considered. It is necessary to verify the specificity of the pH electrode (Figure 3f). Upon adding 100 μM $CaCl_2$, 10 mM KCl, and 100 mM NaCl to a pH 7 PBS buffer solution, interference was observed in the detection signal. However, the potential output change induced by interfering substances was significantly smaller than the response change in the target analyte, underscoring the pH sensor's robust specificity.

3.3. Characterization of Gel

Tensile tests were conducted to assess the mechanical properties of the Gel, demonstrating a stretch capacity of approximately 580%, while its adhesive characteristics were confirmed by the ability to support a 30 g tool (Figure 4a). Figure 4b displays the spectrograms of $AgNO_3$ reacted with and without GL for 10 min under UV irradiation, where the reaction with GL exhibited a distinct peak at 410 nm, contrasting with the absence of peaks in the unreacted control, confirming successful reduction in AgNPs [50,51]. The antibacterial activity of AgNPs was quantitatively assessed against *E. coli* and *S. aureus* (Figure 4c). At 8 μg/mL AgNPs, bacterial reduction rates reached 88.6 ± 3.4% (*E. coli*) and 74.7 ± 4.7% (*S. aureus*) after 24 h. Figure 4c further demonstrates the antibacterial efficacy of AgNPs solutions, revealing significant concentration-dependent inhibition of bacterial proliferation. Cytotoxicity evaluation in Figure 4d showed no significant toxicity to L929 fibroblasts at AgNPs concentrations ≤8 μg/mL (viability comparable to control), while viability markedly decreased at ≥16 μg/mL. Specifically, cytotoxicity tests on L929 fibroblasts confirmed >85.1 ± 6.9% cell viability at AgNPs concentrations ≤8 μg/mL, while viability dropped to 51.6 ± 6.7% at 16 μg/mL. These data validate the potent yet biocompatible antimicrobial function of AgNPs, establishing concentration-dependent cytotoxicity and underscoring the need for precise dosage control to balance antimicrobial efficacy and cellular safety. Concurrently, Figure 4e illustrates the excellent optical transparency of the initial Gel enabling wound visualization, with substantial redness increase after loading rhodamine-B labeled Lipo confirming feasible drug loading via incubation; subsequent color transition from colorless to brownish yellow following $AgNO_3$ coating and redox reaction verified successful in situ AgNPs generation. Finally, Figure 4f presents an SEM image captured at 5000 V accelerating voltage, revealing the internal porous structure at 50 μm scale, where the transparent network and high water content facilitate drug loading through incubation [52–54].

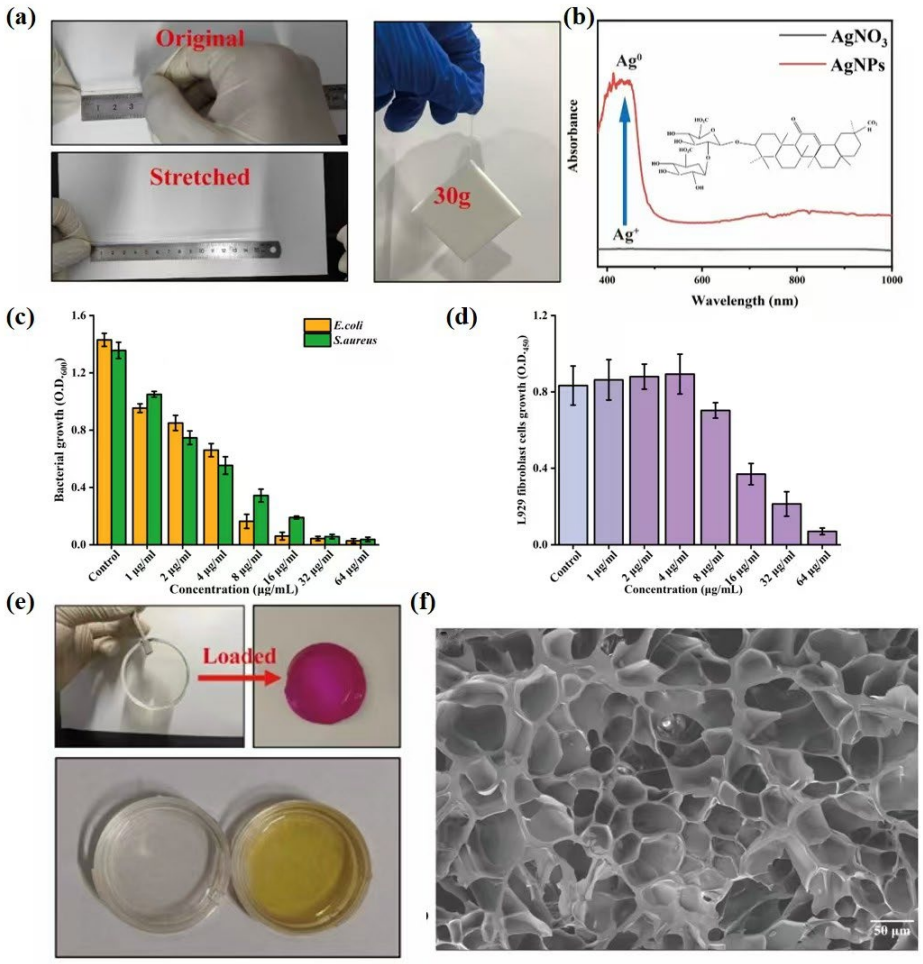


Figure 4. Characterization of Gel. (**a**) Characterization of Gel's stretchability and adhesive properties. (**b**) UV-Vis spectra revealed that GL reacts with Ag^+ to produce AgNPs; (**c**) Growth of two bacterial species measured at OD_{600} under different concentrations of AgNPs for 24 h. (**d**) Growth of L929 fibroblasts was measured at OD_{450} under different concentrations of AgNPs for 24 h. (**e**) Drug loading and in situ reduction in the AgNPs layer on the hydrogel surface. (**f**) SEM image of the Gel.

3.4. Optimization and Characterization of Lipo@Ami

Anionic liposomes were modified to enhance drug release and bacterial binding in wound infections. Drug-coated Lipo was successfully developed by varying the mass ratio of egg yolk lecithin to cholesterol (4:1, 6:1, and 8:1). The zeta potential and polydispersity index (PDI) of Lipo@Ami were investigated by Malvern particle sizer. The standard curve of concentration–absorbance of Ami (Figure S5) and the encapsulation rate of Lipo@Ami at each ratio of formulation were measured by ultracentrifugation. As shown in Figure S6, the liposomes were modified to be positively charged with little change in PDI; the average PDI decreased from 0.276 to 0.241. After embedding Ami, the average PDI was further reduced to 0.153. The zeta potential shifted from negative to positive, with an increase in absolute value to 37.89 after Ami incorporation. The formulation with a cholesterol/yolk lecithin/1-Octadecanamine/Ami = 1.5:12:1.5:2.25 exhibited the highest encapsulation rate of 86.34%. Consequently, this formulation was selected for subsequent experiments.

The ratio of lecithin to cholesterol in liposomes affects the structural stability and drug encapsulation rate. Therefore, it is necessary to optimize the prescription parameters. Liposomes are analogous to cell membranes and comprise a phospholipid bilayer structure. Cholesterol within liposomes provides physical stability by filling the spaces between phospholipid molecules. Furthermore, the lecithin content of liposomes can also affect the fluidity and stability of these structures. Previous studies have examined lecithin-

to-cholesterol ratios ranging from 1:1 to 10:1 [55–57]. Accordingly, the mass ratio of yolk lecithin to cholesterol was 4:1, 6:1, and 8:1 in the preparation of liposomes. The zeta potential can be employed to gauge the stability of the nano-liposomes and thus determine whether aggregation and deposition are occurring within the system. In general, for the particles to resist electrostatic rejection, the zeta potential of the colloidal system must exceed ±30 mV. After adding 1-Octadecanamine and embedding Ami, the PDI of liposomes became smaller, and the dispersion system became more homogeneous [58]. The absolute values of zeta potentials were all higher than 30 mV, indicating that the liposome system had good electrostatic stability [59]. During the preparation of Lipo@Ami, the absolute value of the zeta potential increased with the modification. This indicates the improved stability of liposomes [60]. This is because 1-octadecylamine is a long-chain fatty amine with an amine group ($–NH_2$) at the head. Amines can undergo protonation in aqueous solution, forming ammonium ions with a positive charge ($–NH_3$) [61]. Modification of liposomes with 1-octadecylamine results in an increase in the surface positive charge, as evidenced by a shift in the Zeta potential from negative to positive (Figure S7). Furthermore, an increase in the surface charge density of the Lipo will result in a greater electrostatic repulsion between the liposome particles, thereby enhancing the Zeta potential and improving the system's stability. Notably, the modified positively charged Lipo can be non-specifically targeted to bacteria in infected wounds by electrostatic action [62]. Furthermore, Ami embedded in the aqueous phase is released directly into the bacteria by the fusion of phospholipid bilayers. It has been demonstrated that Lipo can fuse with the outer membrane of Gram-negative bacteria, such as *E. coli*, when in contact with them [63]. In comparison to neutral and negative liposomes, Lipo demonstrates enhanced permeability.

In the formulation of liposomes, precise control over the phospholipid dosage is crucial, with a simultaneous reduction in cholesterol content. This strategy leads to an improved drug encapsulation efficiency, possibly due to the competitive interaction between the hydrophilic drug Ami and cholesterol [64]. The hydrophilic nature of Ami suggests its localization within the aqueous core of the liposomes. It has been hypothesized that higher levels of cholesterol could expand the packing space within the phospholipid bilayer, potentially hindering drug encapsulation. This observation underscores the significance of optimizing parameters on drug encapsulation efficiency, as depicted in Figure S6.

3.5. Electronic Control Gel-Lipo@Ami Drug Release Test

Rhodamine B was added during the preparation of Lipo@Ami (Figure S7) to observe the drug release. Images of the drug released onto the slide were captured by orthogonal fluorescence microscopy. ImageJ analysis was utilized to quantify the Integrated Optical Density (IOD) of the images, which corresponded to the cumulative drug release from Gel-Lipo@Ami. A FPCB was fabricated and integrated with the sensor and Gel-Lipo@Ami. The schematic of the FPCB design is depicted in Figure 5a, with its principle illustrated in Figure S8. The integrated system is approximately 0.5 cm thick and can be worn on the skin. Remote wireless control of the PCB enables the application of precise electrical stimulation to Gel-Lipo@Ami for controlled drug release (Figure 5b). Subsequent investigation on the swelling behavior of the hydrogel revealed that the Gel reached swelling equilibrium within 24 h (Figure 5d). The Gel was sealed in Petri dishes containing fluorescently labeled Lipo@Ami and incubated at 4 °C for 1 h, 4 h, 8 h, and 24 h. It was demonstrated that the drug loading rate of Gel increased in conjunction with the extension of the incubation period, attaining its maximum value at the point of equilibrium, which was observed to occur at 24 h. The maximum loading efficiency was found to be 25.51% (Figure 5e). This suggests that highly porous hydrogel networks under equilibrium swelling conditions can significantly improve drug loading efficiency [65,66].

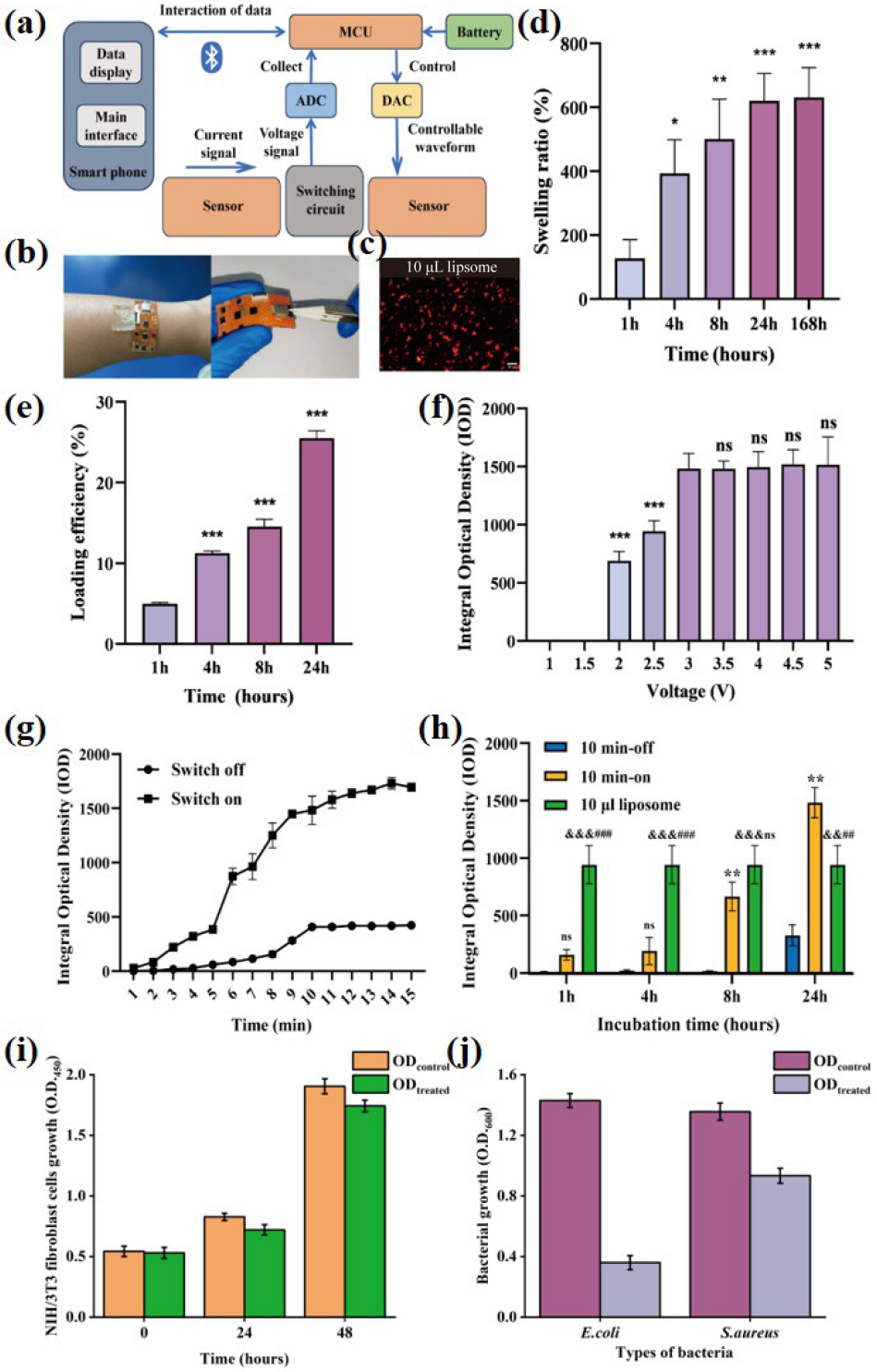


Figure 5. Electronic control Gel-Lipo@Ami drug release test. (**a**) FPCB circuit flow chart. (**b**) Integrated system diagram. (**c**) Image of Lipo@Ami labeled with Rhodamine B (10 μL) under a positive fluorescence microscope. (**d**) Swelling rate of the Gel. (**e**) Gel drug loading rate at different incubation times. (**f**) Cumulative drug release of Gel-Lipo@Ami at different voltages. (**g**) The natural cumulative release of drugs and the cumulative release of drugs under the control of 3 V voltage within 1–15 min. (**h**) At 3 V voltage, Gel incubated for 1–24 h, and the drug was released on/off for 10 min cumulative drug release (10 μL fluorescent liposomes used as the control). * represents the comparison between 10 min-on and 10 min-off; and & represents the comparison between 10 μL liposomes and 10 min-off; # represents the comparison between 10 μL liposomes and 10 min-on. N = 3. (**i**) Effects of hydrogel extract on NIH/3T3 fibroblast proliferation measured at OD_{450} at 24 and 48 h. (**j**) Inhibitory effects of hydrogel extract on *E. coli* and *S. aureus* proliferation measured at OD_{600} within 24 h. (*, &, # represent $p < 0.05$, **, &&, ## represent $p < 0.01$, ***, &&&, ### represent $p < 0.001$, ns represents not significant).

To investigate the voltage and time conditions for controlling drug release, 10 μL Lipo@Ami was used as a reference, and IOD representing the cumulative drug release was used for control experiments (Figure 5c). The release rate of zwitterionic hydrogel is dependent upon the voltage excitation applied externally, thereby enabling the therapeutic module to achieve the desired therapeutic effect of on-demand drug delivery. Electrostatic interactions between the hydrogel matrix, Lipo, and external electric fields may influence the drug release. The electrochemical properties of the Gel can be changed by applying different voltages, and the Gel exhibits a response to swelling or protonation contraction [67]. Applying an electric field force results in the electrophoresis of positively charged Lipo@Ami towards an electrode with an opposite charge, thereby influencing the drug release rate [35]. Consequently, drug release was monitored over a 5 min period at voltages ranging from 1 to 5 V (Figure 5f). Gel-Lipo@Ami cannot accelerate drug release at 1 V and 1.5 V, as the high resistance value of Gel. Following an increase in voltage to 3 V, no significant difference was observed in the cumulative amount of drug released at the same release time. Therefore, 3 V was selected as the voltage at which the excitation was applied for the subsequent experiment.

The release of drugs from Gel is dependent on the application or removal of voltage, resulting in an "on-off" frequency of drug release [30]. To ascertain whether drugs were released dynamically, an investigation was conducted into the cumulative drug release of Gel-Lipo@Ami throughout 1–15 min under the influence of a 3 V voltage excitation (Figure 5g). Upon the application of voltage, the release of Lipo@Ami exhibited a gradual increase over the initial 5 min, followed by a period of accelerated growth between 5 and 9 min. After 10 min, the release rate slowed down. In the absence of voltage, the release of Lipo@Ami displayed a slower initial rate between 1 and 8 min, followed by an accelerated growth phase between 8 and 10 min, and finally reaching a state of equilibrium after 10 min. Thus, 10 min can be chosen as the time to apply the voltage. Finally, the "on-off" voltage release of Lipo@Ami at 3 V for 10 min from 1 to 24 h of incubation time was examined using 10 μL of rhodamine B-labeled Lipo@Ami as a control (Figure 5h). The natural drug release amount of Gel-Lipo@Ami, which did not reach the swelling equilibrium, was negligible. In contrast, the IOD value of Gel-Lipo@Ami, which reached the swelling equilibrium, was approximately 300. The drug release of Gel-Lipo@Ami incubated for 1–24 h under 3 V voltage excitation showed an increasing trend. It exceeded the IOD value of the control group at 24 h of incubation. Fluorograms of drug release for each group are shown in Figure S9a,b shows comparisons between natural release, control release, and control samples within each group. Consequently, incubating Gel-Lipo@Ami prepared for 24 h under 3 V voltage for 10 min emerged as a viable protocol for subsequent animal experiments.

Given the above findings on drug release characteristics, it is crucial to evaluate the antibacterial and biocompatibility properties of the hydrogel to ensure its safety and efficacy in practical applications. Results of hydrogel antibacterial and biocompatibility tests indicated that over the 0–48 h period, both $OD_{control}$ and $OD_{treated}$ groups exhibited significant promotive effects on NIH/3T3 fibroblast proliferation (Figure 5i). However, the $OD_{treated}$ values were consistently lower than those of $OD_{control}$. This difference may be attributed to minimal inhibitory effects on NIH/3T3 fibroblasts resulting from AgNPs release from the hydrogel extract. Concurrently, hydrogel antibacterial assays demonstrated significantly reduced proliferation efficiency in both bacterial strains following treatment with hydrogel extracts (Figure 5j). Hydrogel extracts exhibited 74.8 ± 3.2% inhibition against *E. coli* and 30.9 ± 5.1% inhibition against *S. aureus* (Figure 5j), confirming selective targeting of bacteria over host cells. It is noteworthy that the potent inhibition against *E. coli* (74.8%) arises from the synergistic action of AgNPs and Ami, as Ami is effective in

clearing Gram-negative *E. coli*. Conversely, the comparatively weaker inhibition against *S. aureus* (30.9%) is primarily attributed to the limited efficacy of Ami against Gram-positive *S. aureus*, where the antibacterial activity relies more heavily on AgNPs alone. These findings confirm that the hydrogel effectively inhibits the proliferation of *E. coli* and *S. aureus* upon wound contact, thereby mitigating infection risks.

3.6. Integrated System Promotes In Vivo Evaluation of Infected Wound Healing

UA concentrations below 220 μM may be associated with bacteria such as *E. coli*, *S. aureus*, and PA in the wound. A study from the 2008 Wenchuan earthquake in Sichuan province showed that up to 46.9 percent of patients in the disaster had *E. coli* infections [68]. Therefore, *E. coli* was selected to simulate wound infection in an emergency environment for wound modeling in rats. The effect of infected wound healing was studied in the untreated group compared to the electro-controlled drug release group (Figure S10). The impact of an integrated electrically controlled drug release system on wound healing was evaluated in a rat wound model that simulated infection with *E. coli*.

The tests were divided into control and treatment groups. The control group was not treated after the wound infection was modeled, and the treatment group was treated based on the previous test results by applying a voltage of 3 V through the PCB for 10 min per treatment. The results of the animal experiments showed that after wound modeling, healing was slower and still incomplete in the control group on day 15. The treatment group had a significantly higher closure rate of wound healing and almost complete healing on day 15 (Figure 6a). The infection prolongs the duration of inflammation during the four stages of wound healing [69]. The wound healing trace map and the wound healing area statistical map, obtained by ImageJ, facilitate a more intuitive analysis of the wound healing situation of the two groups (Figure 6b,c). Wound healing was accelerated in the treated group after the seventh day, indicating that electrical stimulation Gel-Lipo@Ami can accelerate the transformation of the wound from the inflammation stage to the tissue healing stage [70,71]. The effect of Gel-Lipo@Ami on the healing of infected wounds can be seen by observing the skin tissue sections of the experimental and treatment groups by H&E staining. The results of H&E staining showed that the skin tissue of the control group still had partial defects and inflammatory tissue infiltration 15 days after the wound modeling. In the treatment group, the skin tissue structure was intact, and there was neocapillogenesis (Figure 6d,e). It is imperative that the dressing is biocompatible to prevent any additional damage to the wound as a result of contact between the dressing and the wound itself. This was studied through H&E staining. The *in vivo* evaluation of the integrated system showed no significant difference in the section results of heart, liver, spleen, lungs, and kidneys between the control group and the treatment group, indicating the good biocompatibility of the material (Figure 6f).

3.7. Coordinated Wound Repair Systems

The integrated system orchestrates wound healing through three synergistic biological systems:

3.7.1. Infection–Inflammation Control System

On-demand Ami release rapidly eliminates pathogens, disrupting the "infection–inflammation" vicious cycle, while concurrently silver ions (Ag^+) from the hydrogel suppress pro-inflammatory cytokine cascades. Furthermore, electrically guided liposome migration enables targeted drug delivery to infection foci, ensuring precise therapeutic intervention.

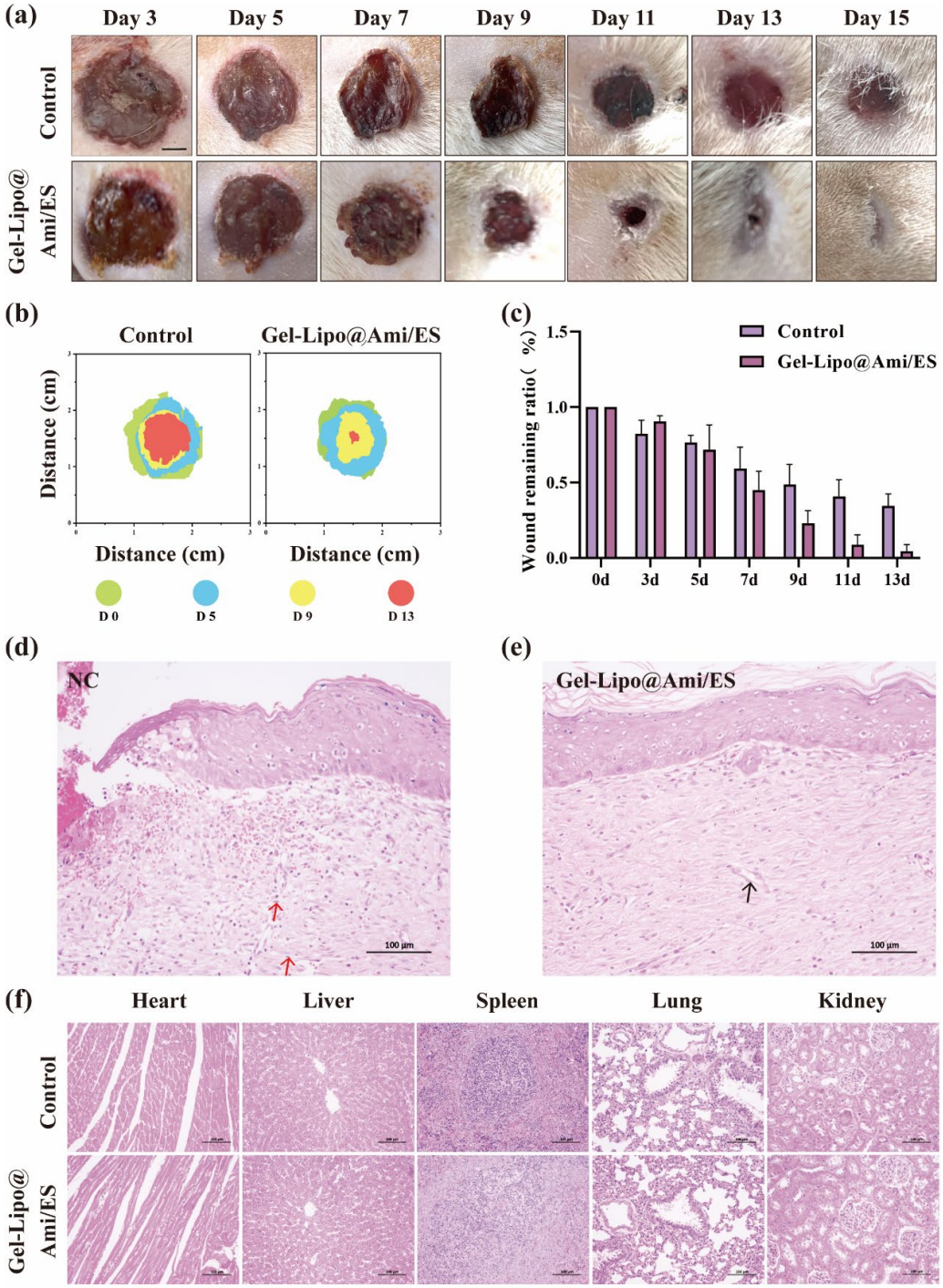


Figure 6. In vivo anti-infective treatment with Gel-Lipo@Ami on a wound infected with *E. coli*. (**a**) Representative images of the control and treatment groups 1 to 15 days after successful wound modeling. Scale bar, 500 mm. (**b**) Wound healing traces of *E. coli* infection in control and treatment groups. (**c**) Quantitative analysis of wound closure in control and treatment groups. (**d**) Representative images of H&E staining of infected skin wounds 15 days later in the control group. (**e**) Representative images of H&E staining of infected skin wounds after 15 days in the treatment group. (**f**) Evaluation of in vivo therapeutic effect after 15 days in the control and treatment groups.

3.7.2. Extracellular Matrix Restoration System

Hydrogel swelling maintains optimal hydration to prevent tissue desiccation and facilitate fibroblast migration, with controlled infection reducing protease-mediated collagen degradation. The zwitterionic polymers further provide biomimetic interfaces that accelerate granulation tissue formation through enhanced cell–matrix interactions.

3.7.3. Angiogenic Revascularization System

Infection clearance alleviates hypoxia to activate vascular endothelial growth signaling, where cationic liposomes electrostatically accumulate at neovascularization sites. This process is structurally supported by the macroporous hydrogel architecture, guiding endothelial cell alignment and capillary network assembly.

4. Conclusions

In summary, this study successfully developed a flexible, stretchable, and wearable closed-loop system for emergency medical rescues, which integrates the real-time multiparametric monitoring of UA, pH, and temperature with electronically controlled on-demand drug release, offering a one-stop strategy for pre-diagnosis and treatment of post-disaster patients. Crucially, it overcomes the limitations of conventional antibiotic dressings by replacing their preset continuous drug-release mode, which ignores actual wound conditions, causing drug waste, underdosing, and temporal mismatches. This system rapidly releases sufficient drugs only upon detection of infection biomarkers and halts release in their absence, minimizing antibiotic misuse, unnecessary exposure, and resistance risks while extending operational duration. In clinical settings, key challenges include long-term bio-stability of the hydrogel under dynamic physiological conditions and conducting cost–benefit analyses for emergency deployment in resource-limited settings. Our work is promising for the embedding of low-power wireless modules for real-time telemedicine and the integration of cloud-based deep learning models for the analysis of multi-parameter dynamics, enabling predictive wound assessment beyond static thresholds. This closed-loop paradigm synergizes precise sensing, adaptive treatment, and data-driven decisions, establishing a transformative approach to emergency wound management.

Supplementary Materials: The following supporting information can be downloaded at: https://www.mdpi.com/article/10.3390/chemosensors13070267/s1. Figure S1: The template design diagram of screen printing electrode (SPE). Figure S2: Flowchart of preparation of SPE. Figure S3: (a) Synthetic Workflow of AgNPs-Functionalized Zwitterionic Conductive Hydrogel. (b) Fabrication Procedure of the Therapeutic Module (Gel-Lipo@Ami). Figure S4: UA concentration gradients and linear fitting of WE modified with GO-COOH: HAuCl4 volume ratios of 10:1, 20:1, and 30:1. Figure S5: Concentration-absorbance curves of amikacin standards. Figure S6: Optimization of liposome parameters. Figure S7: Physical diagram of the Tyndall effect of Lipo@Ami and rhodamine B-labeled Lipo@Ami. Figure S8: The schematic diagram of PCB. Figure S9: (a) Fluorograms of Gel-Lipo@Ami incubated for 1–24 h. (b) Comparison of cumulative drug release of Gel-Lipo@Ami at different incubation times. Figure S10: Flowchart of animal experiment.

Author Contributions: Conceptualization, S.L. and Z.C.; data curation, Z.Y.; formal analysis, W.L. and B.F.; funding acquisition, S.L. and Z.C.; investigation, Q.C. and L.D.; methodology, S.W., S.H., W.L. and H.L.; project administration, B.F. and Z.C.; resources, B.F.; software, S.H. and Z.Y.; supervision, Z.C.; validation, Q.C., L.D. and H.L.; visualization, B.F.; writing—original draft, S.W. and S.H.; writing—review and editing, S.H. and Y.L. All authors have read and agreed to the published version of the manuscript.

Funding: This research was funded by the National Key Research and Development Program of China (grant number 2023YFC3011802), the Zhejiang Provincial Natural Science Foundation of China (grant number LMS25H180006), the National Natural Science Foundation of China (grant number 82001922, 22274110, and 22250610197), the Tianjin Education Commission Scientific Research Program (grant number 2023YXZX12), the Hong Kong Scholars Program (grant number XJ2021034), and the Independent Innovation Fund of Tianjin University (grant number 2023XJS-0076).

Institutional Review Board Statement: The animal study was approved by the Experimental Animal Ethics Committee of Tianjin University (protocol code 20250113001 and approved by 13 January 2025).

Informed Consent Statement: Not applicable.

Data Availability Statement: Data will be made available on request.

Conflicts of Interest: The authors declare that they have no known competing financial interests or personal relationships that could have appeared to influence the work reported in this paper.

Abbreviations

The following abbreviations are used in this manuscript:

UA	Uric acid
AgNPs	Silver nanoparticles
SBMA	[2-(Methacryloyloxy)ethyl]dimethyl-(3-sulfopropyl)ammonium hydroxide
HEAA	N-(2-Hydroxyethyl)-2-acrylamide
GL	Glycyrrhizic acid
CV	Cyclic voltammetry
DPV	Differential pulse voltammetry
IOD	Integrated optical density
SEM	Scanning electron microscopy
Ami	Amikacin
Lipo	Cationic liposomes
Gel	Zwitterionic conductive hydrogel
E. coli	*Escherichia coli*
S. aureus	*Staphylococcus aureus*
FPCB	Flexible printed circuit board
CCK-8	Cell counting kit-8
CE	Counter electrode
RE	Reference electrode
WE	Working electrode
PVB	Polyvinyl Butyral
OCPT	Open circuit potential-time
OD	Optical density
ATP	Adenosine triphosphate
ROS	Reactive oxygen species
PA	Pseudomonas aeruginosa
PANI	Polyaniline

References

1. Percival, S.L.; Emanuel, C.; Cutting, K.F.; Williams, D.W. Microbiology of the skin and the role of biofilms in infection. *Int. Wound J.* **2012**, *9*, 14–32. [CrossRef]
2. Zhu, J.; Cheng, H.; Zhang, Z.; Chen, K.; Zhang, Q.; Zhang, C.; Gao, W.; Zheng, Y. Antibacterial hydrogels for wound dressing applications: Current status, progress, challenges, and trends. *Gels* **2024**, *10*, 495. [CrossRef] [PubMed]
3. Murray, C.J.; Ikuta, K.S.; Sharara, F.; Swetschinski, L.; Aguilar, G.R.; Gray, A.; Han, C.; Bisignano, C.; Rao, P.; Wool, E.; et al. Global burden of bacterial antimicrobial resistance in 2019: A systematic analysis. *Lancet* **2022**, *399*, 629–655. [CrossRef] [PubMed]
4. Mohamed Salleh, N.A.B.; Tanaka, Y.; Sutarlie, L.; Su, X. Detecting bacterial infections in wounds: A review of biosensors and wearable sensors in comparison with conventional laboratory methods. *Analyst* **2022**, *147*, 1756–1776. [CrossRef] [PubMed]
5. Yu, P.; Wei, L.; Yang, Z.; Liu, X.; Ma, H.; Zhao, J.; Liu, L.; Wang, L.; Chen, R.; Cheng, Y. Hydrogel wound dressings accelerating healing process of wounds in movable parts. *Int. J. Mol. Sci.* **2024**, *25*, 6610. [CrossRef]
6. Valdez, M.K.; Sexton, J.D.; Lutz, E.A.; Reynolds, K.A. Spread of infectious microbes during emergency medical response. *Am. J. Infect. Control* **2015**, *43*, 606–611. [CrossRef]
7. Lu, S.-H.; Samandari, M.; Li, C.; Li, H.; Song, D.; Zhang, Y.; Tamayol, A.; Wang, X. Multimodal sensing and therapeutic systems for wound healing and management: A review. *Sens. Actuators Rep.* **2022**, *4*, 100075. [CrossRef]
8. Guo, J. Uric Acid Monitoring with a Smartphone as the Electrochemical Analyzer. *Anal. Chem.* **2016**, *88*, 11986–11989. [CrossRef]
9. Liu, X.; Lillehoj, P.B. Embroidered electrochemical sensors on gauze for rapid quantification of wound biomarkers. *Biosens. Bioelectron.* **2017**, *98*, 189–194. [CrossRef]

10. Yapor, J.P.; Alharby, A.; Gentry-Weeks, C.; Reynolds, M.M.; Alam, A.; Li, Y.V. Polydiacetylene Nanofiber Composites as a Colorimetric Sensor Responding To Escherichia coli and pH. *ACS Omega* **2017**, *2*, 7334–7342. [CrossRef]
11. Chanmugam, A.; Langemo, D.; Thomason, K.; Haan, J.; Altenburger, E.A.; Tippett, A.; Henderson, L.; Zortman, T.A. Relative Temperature Maximum in Wound Infection and Inflammation as Compared with a Control Subject Using Long-Wave Infrared Thermography. *Adv. Skin Wound Care* **2017**, *30*, 406–414. [CrossRef]
12. Zhang, Z.; Su, R.; Han, F.; Zheng, Z.; Liu, Y.; Zhou, X.; Li, Q.; Zhai, X.; Wu, J.; Pan, X.; et al. A soft intelligent dressing with pH and temperature sensors for early detection of wound infection. *RSC Adv.* **2022**, *12*, 3243–3252. [CrossRef]
13. Youssef, K.; Ullah, A.; Rezai, P.; Hasan, A.; Amirfazli, A. Recent advances in biosensors for real time monitoring of pH, temperature, and oxygen in chronic wounds. *Mater. Today Bio* **2023**, *22*, 100764. [CrossRef]
14. Fernandez, M.L.; Upton, Z.; Edwards, H.; Finlayson, K.; Shooter, G.K. Elevated uric acid correlates with wound severity. *Int. Wound J.* **2012**, *9*, 139–149. [CrossRef]
15. Bessa, L.J.; Fazii, P.; Di Giulio, M.; Cellini, L. Bacterial isolates from infected wounds and their antibiotic susceptibility pattern: Some remarks about wound infection. *Int. Wound J.* **2015**, *12*, 47–52. [CrossRef] [PubMed]
16. Yang, C.; Zhang, Z.; Gan, L.; Zhang, L.; Yang, L.; Wu, P. Application of Biomedical Microspheres in Wound Healing. *Int. J. Mol. Sci.* **2023**, *24*, 7319. [CrossRef] [PubMed]
17. Liu, W.; Wang, M.; Cheng, W.; Niu, W.; Chen, M.; Luo, M.; Xie, C.; Leng, T.; Zhang, L.; Lei, B. Bioactive antiinflammatory antibacterial hemostatic citrate-based dressing with macrophage polarization regulation for accelerating wound healing and hair follicle neogenesis. *Bioact. Mater.* **2021**, *6*, 721–728. [CrossRef]
18. Song, J.W.; Ryu, H.; Bai, W.; Xie, Z.; Vázquez-Guardado, A.; Nandoliya, K.; Avila, R.; Lee, G.; Song, Z.; Kim, J.; et al. Bioresorbable, wireless, and battery-free system for electrotherapy and impedance sensing at wound sites. *Sci. Adv.* **2023**, *9*, eade4687. [CrossRef]
19. Zhao, Y.; Wang, X.; Qi, R.; Yuan, H. Recent Advances of Natural-Polymer-Based Hydrogels for Wound Antibacterial Therapeutics. *Polymers* **2023**, *15*, 3305. [CrossRef]
20. Wang, S.; Zheng, H.; Zhou, L.; Cheng, F.; Liu, Z.; Zhang, H.; Zhang, Q. Injectable redox and light responsive MnO(2) hybrid hydrogel for simultaneous melanoma therapy and multidrug-resistant bacteria-infected wound healing. *Biomaterials* **2020**, *260*, 120314. [CrossRef]
21. Mostafalu, P.; Tamayol, A.; Rahimi, R.; Ochoa, M.; Khalilpour, A.; Kiaee, G.; Yazdi, I.K.; Bagherifard, S.; Dokmeci, M.R.; Ziaie, B.; et al. Smart Bandage for Monitoring and Treatment of Chronic Wounds. *Small* **2018**, *14*, e1703509. [CrossRef] [PubMed]
22. Guan, L.; Ou, X.; Wang, Z.; Li, X.; Feng, Y.; Yang, X.; Qu, W.; Yang, B.; Lin, Q. Electrical stimulation-based conductive hydrogel for immunoregulation, neuroregeneration and rapid angiogenesis in diabetic wound repair. *Sci. China Mater.* **2023**, *66*, 1237–1248. [CrossRef]
23. Yang, J.; Wang, Z.; Ma, C.; Tang, H.; Hao, H.; Li, M.; Luo, X.; Yang, M.; Gao, L.; Li, J. Advances in Hydrogels of Drug Delivery Systems for the Local Treatment of Brain Tumors. *Gels* **2024**, *10*, 404. [CrossRef] [PubMed]
24. Gamboa, J.; Paulo-Mirasol, S.; Estrany, F.; Torras, J. Recent Progress in Biomedical Sensors Based on Conducting Polymer Hydrogels. *ACS Appl. Bio Mater.* **2023**, *6*, 1720–1741. [CrossRef]
25. Stevens, D.L.; Aldape, M.J.; Bryant, A.E. Life-threatening clostridial infections. *Anaerobe* **2012**, *18*, 254–259. [CrossRef]
26. Zhang, B.; Liu, Z.; Lin, Z.; Zhang, X.; Fu, W. Microbiologic characteristics of pathogenic bacteria from hospitalized trauma patients who survived Wenchuan earthquake. *Eur. J. Clin. Microbiol. Infect. Dis.* **2012**, *31*, 2529–2535. [CrossRef]
27. Feng, W.; Wang, Z. Tailoring the Swelling-Shrinkable Behavior of Hydrogels for Biomedical Applications. *Adv. Sci.* **2023**, *10*, e2303326. [CrossRef]
28. Lazaridou, M.; Nanaki, S.; Zamboulis, A.; Papoulia, C.; Chrissafis, K.; Klonos, P.A.; Kyritsis, A.; Vergkizi-Nikolakaki, S.; Kostoglou, M.; Bikiaris, D.N. Super absorbent chitosan-based hydrogel sponges as carriers for caspofungin antifungal drug. *Int. J. Pharm.* **2021**, *606*, 120925. [CrossRef]
29. Zhao, F.; Yao, D.; Guo, R.; Deng, L.; Dong, A.; Zhang, J. Composites of Polymer Hydrogels and Nanoparticulate Systems for Biomedical and Pharmaceutical Applications. *Nanomaterials* **2015**, *5*, 2054–2130. [CrossRef]
30. Shirzaei Sani, E.; Xu, C.; Wang, C.; Song, Y.; Min, J.; Tu, J.; Solomon, S.A.; Li, J.; Banks, J.L.; Armstrong, D.G.; et al. A stretchable wireless wearable bioelectronic system for multiplexed monitoring and combination treatment of infected chronic wounds. *Sci. Adv.* **2023**, *9*, eadf7388. [CrossRef]
31. Liu, W.S.; Liu, Y.; Gao, J.; Zheng, H.; Lu, Z.M.; Li, M. Biomembrane-Based Nanostructure- and Microstructure-Loaded Hydrogels for Promoting Chronic Wound Healing. *Int. J. Nanomed.* **2023**, *18*, 385–411. [CrossRef]
32. Zhang, H.; Tang, N.; Yu, X.; Guo, Z.; Liu, Z.; Sun, X.; Li, M.-H.; Hu, J. Natural glycyrrhizic acid-tailored hydrogel with in-situ gradient reduction of AgNPs layer as high-performance, multi-functional, sustainable flexible sensors. *Chem. Eng. J.* **2022**, *430*, 132779. [CrossRef]
33. Zhang, T.; Qin, X.; Gao, Y.; Kong, D.; Jiang, Y.; Cui, X.; Guo, M.; Chen, J.; Chang, F.; Zhang, M.; et al. Functional chitosan gel coating enhances antimicrobial properties and osteogenesis of titanium alloy under persistent chronic inflammation. *Front. Bioeng. Biotechnol.* **2023**, *11*, 1118487. [CrossRef]

34. Yi, Y.T.; Sun, J.Y.; Lu, Y.W.; Liao, Y.C. Programmable and on-demand drug release using electrical stimulation. *Biomicrofluidics* **2015**, *9*, 022401. [CrossRef] [PubMed]
35. Nowak, M.; Barańska-Rybak, W. Nanomaterials as a Successor of Antibiotics in Antibiotic-Resistant, Biofilm Infected Wounds? *Antibiotics* **2021**, *10*, 941. [CrossRef] [PubMed]
36. Talló, K.; Vílchez, S.; Pons, R.; López, O. Gels formed from the interaction of lipid vesicles: Influence of charge in their structural and rheological properties. *J. Mol. Liq.* **2021**, *322*, 114957. [CrossRef]
37. Mukherjee, A.; Lodha, R.; Kabra, S.K. Current therapies for the treatment of multidrug-resistant tuberculosis in children in India. *Expert Opin. Pharmacother.* **2017**, *18*, 1595–1606. [CrossRef]
38. Rukavina, Z.; Vanić, Ž. Current Trends in Development of Liposomes for Targeting Bacterial Biofilms. *Pharmaceutics* **2016**, *8*, 18. [CrossRef]
39. Zhou, T.; Liu, Y.; Lei, K.; Liu, J.; Hu, M.; Guo, L.; Guo, Y.; Ye, Q. A "Trojan Horse" Strategy: The Preparation of Bile Acid-Modifying Irinotecan Hydrochloride Nanoliposomes for Liver-Targeted Anticancer Drug Delivery System Study. *Molecules* **2023**, *28*, 1577. [CrossRef]
40. Fernandez, M.L.; Upton, Z.; Shooter, G.K. Uric acid and xanthine oxidoreductase in wound healing. *Curr. Rheumatol. Rep.* **2014**, *16*, 396. [CrossRef]
41. Mirzaei, Y.; Hagemeister, K.; Hüffel, M.; Schwandt, T.; Tolba, R.H.; Steitz, J. A Novel *In Vitro* Method to Assess the Microbial Barrier Function of Tissue Adhesives Using Bioluminescence Imaging Technique. *Biomed. Res. Int.* **2022**, *2022*, 3483238. [CrossRef] [PubMed]
42. Kapusta, O.; Jarosz, A.; Stadnik, K.; Giannakoudakis, D.A.; Barczyński, B.; Barczak, M. Antimicrobial Natural Hydrogels in Biomedicine: Properties, Applications, and Challenges-A Concise Review. *Int. J. Mol. Sci.* **2023**, *24*, 2191. [CrossRef] [PubMed]
43. Wysocki, A.B.; Bhalla-Regev, S.K.; Tierno, P.M., Jr.; Stevens-Riley, M.; Wiygul, R.C. Proteolytic activity by multiple bacterial species isolated from chronic venous leg ulcers degrades matrix substrates. *Biol. Res. Nurs.* **2013**, *15*, 407–415. [CrossRef]
44. Arcangeli, D.; Gualandi, I.; Mariani, F.; Tessarolo, M.; Ceccardi, F.; Decataldo, F.; Melandri, F.; Tonelli, D.; Fraboni, B.; Scavetta, E. Smart Bandaid Integrated with Fully Textile OECT for Uric Acid Real-Time Monitoring in Wound Exudate. *ACS Sens.* **2023**, *8*, 1593–1608. [CrossRef] [PubMed]
45. Tong, Y.; Wei, Y.; Ju, Y.; Li, P.; Zhang, Y.; Li, L.; Gao, L.; Liu, S.; Liu, D.; Hu, Y.; et al. Anaerobic purinolytic enzymes enable dietary purine clearance by engineered gut bacteria. *Cell Chem. Biol.* **2023**, *30*, 1104–1114.e1107. [CrossRef]
46. Ji, D.; Liu, Z.; Liu, L.; Low, S.S.; Lu, Y.; Yu, X.; Zhu, L.; Li, C.; Liu, Q. Smartphone-based integrated voltammetry system for simultaneous detection of ascorbic acid, dopamine, and uric acid with graphene and gold nanoparticles modified screen-printed electrodes. *Biosens. Bioelectron.* **2018**, *119*, 55–62. [CrossRef]
47. Cullen, B.; Gefen, A. The biological and physiological impact of the performance of wound dressings. *Int. Wound J.* **2023**, *20*, 1292–1303. [CrossRef]
48. Sun, X.; Zhang, Y.; Ma, C.; Yuan, Q.; Wang, X.; Wan, H.; Wang, P. A Review of Recent Advances in Flexible Wearable Sensors for Wound Detection Based on Optical and Electrical Sensing. *Biosensors* **2021**, *12*, 10. [CrossRef]
49. Mariani, F.; Serafini, M.; Gualandi, I.; Arcangeli, D.; Decataldo, F.; Possanzini, L.; Tessarolo, M.; Tonelli, D.; Fraboni, B.; Scavetta, E. Advanced Wound Dressing for Real-Time pH Monitoring. *ACS Sens.* **2021**, *6*, 2366–2377. [CrossRef]
50. Lin, G.; Zhao, C.; Liao, W.; Yang, J.; Zheng, Y. Eco-Friendly Green Synthesis of Rubropunctatin Functionalized Silver Nanoparticles and Evaluation of Antibacterial Activity. *Nanomaterials* **2022**, *12*, 4052. [CrossRef]
51. Widatalla, H.A.; Yassin, L.F.; Alrasheid, A.A.; Rahman Ahmed, S.A.; Widdatallah, M.O.; Eltilib, S.H.; Mohamed, A.A. Green synthesis of silver nanoparticles using green tea leaf extract, characterization and evaluation of antimicrobial activity. *Nanoscale Adv.* **2022**, *4*, 911–915. [CrossRef] [PubMed]
52. Sun, X.; Liu, D.; Xu, X.; Shen, Y.; Huang, Y.; Zeng, Z.; Xia, M.; Zhao, C. NIR-triggered thermo-responsive biodegradable hydrogel with combination of photothermal and thermodynamic therapy for hypoxic tumor. *Asian J. Pharm. Sci.* **2020**, *15*, 713–727. [CrossRef] [PubMed]
53. Dobashi, T. Shaping and Structuring of Polymer Gels. *Gels* **2024**, *10*, 134. [CrossRef] [PubMed]
54. Yao, J.; Song, S.; Zhao, H.; Yuan, Y. Platinum-based drugs and hydrogel: A promising anti-tumor combination. *Drug. Deliv.* **2023**, *30*, 2287966. [CrossRef]
55. Chen, Z.; Zhao, Y.Y.; Li, L.; Li, Z.; Fu, S.; Xu, Y.; Zheng, B.Y.; Ke, M.; Li, X.; Huang, J.D. A Sulfur-Bridging Sulfonate-Modified Zinc(II) Phthalocyanine Nanoliposome Possessing Hybrid Type I and Type II Photoreactions with Efficient Photodynamic Anticancer Effects. *Molecules* **2023**, *28*, 2250. [CrossRef]
56. Salem, H.F.; Ahmed, S.M.; Hassaballah, A.E.; Omar, M.M. Targeting brain cells with glutathione-modulated nanoliposomes: *In vitro* and *in vivo* study. *Drug. Des. Devel. Ther.* **2015**, *9*, 3705–3727. [CrossRef]
57. Qi, N.; Tang, B.; Liu, G.; Liang, X. Poly(γ-glutamic acid)-coated lipoplexes loaded with Doxorubicin for enhancing the antitumor activity against liver tumors. *Nanoscale Res. Lett.* **2017**, *12*, 361. [CrossRef]

58. Tsichlis, I.; Manou, A.P.; Manolopoulou, V.; Matskou, K.; Chountoulesi, M.; Pletsa, V.; Xenakis, A.; Demetzos, C. Development of Liposomal and Liquid Crystalline Lipidic Nanoparticles with Non-Ionic Surfactants for Quercetin Incorporation. *Materials* **2023**, *16*, 5509. [CrossRef]
59. Feng, L.; Ye, W.; Zhang, K.; Qu, D.; Liu, W.; Wu, M.; Han, J. In vitro Digestion Characteristics of Hydrolyzed Infant Formula and Its Effects on the Growth and Development in Mice. *Front. Nutr.* **2022**, *9*, 912207. [CrossRef]
60. Gu, X.; Wang, D.; Wang, X.; Liu, Y.; Di, X. Fast Screening of Biomembrane-Permeable Compounds in Herbal Medicines Using Bubble-Generating Magnetic Liposomes Coupled with LC-MS. *Molecules* **2021**, *26*, 1742. [CrossRef]
61. Li, M.; Xu, J.; Pei, D.; Su, K.; Wang, L. Evaluation of Aminated Nano-Silica as a Novel Shale Stabilizer to Improve Wellbore Stability. *Materials* **2024**, *17*, 1776. [CrossRef]
62. Liu, Y.; Shi, L.; Su, L.; van der Mei, H.C.; Jutte, P.C.; Ren, Y.; Busscher, H.J. Nanotechnology-based antimicrobials and delivery systems for biofilm-infection control. *Chem. Soc. Rev.* **2019**, *48*, 428–446. [CrossRef]
63. Scheeder, A.; Brockhoff, M.; Ward, E.N.; Kaminski Schierle, G.S.; Mela, I.; Kaminski, C.F. Molecular Mechanisms of Cationic Fusogenic Liposome Interactions with Bacterial Envelopes. *J. Am. Chem. Soc.* **2023**, *145*, 28240–28250. [CrossRef] [PubMed]
64. Briuglia, M.L.; Rotella, C.; McFarlane, A.; Lamprou, D.A. Influence of cholesterol on liposome stability and on *in vitro* drug release. *Drug. Deliv. Transl. Res.* **2015**, *5*, 231–242. [CrossRef] [PubMed]
65. Udeni Gunathilake, T.M.S.; Ching, Y.C.; Chuah, C.H. Enhancement of Curcumin Bioavailability Using Nanocellulose Reinforced Chitosan Hydrogel. *Polymers* **2017**, *9*, 64. [CrossRef] [PubMed]
66. Wei, S.; Ching, Y.C.; Chuah, C.H. Synthesis of chitosan aerogels as promising carriers for drug delivery: A review. *Carbohydr. Polym.* **2020**, *231*, 115744. [CrossRef]
67. Municoy, S.; Álvarez Echazú, M.I.; Antezana, P.E.; Galdopórpora, J.M.; Olivetti, C.; Mebert, A.M.; Foglia, M.L.; Tuttolomondo, M.V.; Alvarez, G.S.; Hardy, J.G.; et al. Stimuli-Responsive Materials for Tissue Engineering and Drug Delivery. *Int. J. Mol. Sci.* **2020**, *21*, 4724. [CrossRef]
68. Wang, Y.; Hao, P.; Lu, B.; Yu, H.; Huang, W.; Hou, H.; Dai, K. Causes of infection after earthquake, China, 2008. *Emerg. Infect. Dis.* **2010**, *16*, 974–975. [CrossRef]
69. Ge, Y.; Wang, Q. Current research on fungi in chronic wounds. *Front. Mol. Biosci.* **2022**, *9*, 1057766. [CrossRef]
70. Du, Y.; Du, W.; Lin, D.; Ai, M.; Li, S.; Zhang, L. Recent Progress on Hydrogel-Based Piezoelectric Devices for Biomedical Applications. *Micromachines* **2023**, *14*, 167. [CrossRef]
71. Cao, J.; Wu, B.; Yuan, P.; Liu, Y.; Hu, C. Rational Design of Multifunctional Hydrogels for Wound Repair. *J. Funct. Biomater.* **2023**, *14*, 553. [CrossRef]

Disclaimer/Publisher's Note: The statements, opinions and data contained in all publications are solely those of the individual author(s) and contributor(s) and not of MDPI and/or the editor(s). MDPI and/or the editor(s) disclaim responsibility for any injury to people or property resulting from any ideas, methods, instructions or products referred to in the content.